Science Advances
AAAS

advances.sciencemag.org/cgi/content/full/5/2/eaau3407/DC1

Supplementary Materials for

Imaging of local structures affecting electrical transport properties of large graphene sheets by lock-in thermography

H. Nakajima, T. Morimoto*, Y. Okigawa, T. Yamada, Y. Ikuta, K. Kawahara, H. Ago, T. Okazaki*

*Corresponding author. Email: t-morimoto@aist.go.jp (T.M.); toshi.okazaki@aist.go.jp (T.O.)

Published 1 February 2019, *Sci. Adv.* **5**, eaau3407 (2019)
DOI: 10.1126/sciadv.aau3407

This PDF file includes:

Section S1. Characterization of polycrystalline graphene sheets
Section S2. Wrinkle in polycrystalline graphene
Section S3. Characterization of epitaxially grown graphene sheets
Section S4. Numerical simulation of Joule heat image of graphene sheets
Section S5. Structural characterization of DB
Section S6. Speed of LIT imaging
Section S7. Heat broadening of LIT measurement in graphene films
Section S8. Direction of defects in LIT measurement
Fig. S1. Optical microscopy image, Raman spectrum, and SEM image of polycrystalline graphene.
Fig. S2. Structural and optical characterization of wrinkle in polycrystalline graphene.
Fig. S3. Optical microscopy image of epitaxially grown graphene domains.
Fig. S4. Micro-Raman spectroscopy with epitaxially grown graphene.
Fig. S5. Simulation of Joule heat imaging.
Fig. S6. Structural analysis of overlapped boundary defect.
Fig. S7. LIT image dependence on data accumulation time.
Fig. S8. Cross-sectional analysis of thermal pattern of LIT.
Fig. S9. Effect of the direction of defects in LIT measurements.
Table S1. Fitting results of Raman spectrum with polycrystalline graphene.

Supplementary Text

Section S1. Characterization of polycrystalline graphene sheets

Figure S1A shows a typical optical microscope image of polycrystalline graphene film transferred onto a quartz substrate. Such images do not reveal the presence of structural damage such as contamination, cracks, tears, or wrinkles. Figure S1B corresponds to the Raman spectra from three excitation points within the film. The 2D-band peak around 2690 cm^{-1} has a symmetric spectral shape with a narrow line width of less than 30 cm^{-1}. A high I_{2D}/I_G and the low I_D/I_G were obtained, as shown in Table S1. These results indicate that the sample consisted of a single layer of graphene (*6*).

The domain size of polycrystalline graphene was estimated from the SEM measurements. Figure S1C-F shows SEM images of a graphene surface at magnifications of x4,000 (Fig. S1C and D) and x12,000 (Fig. S1E and F). The region with low contrast corresponds to single-layer graphene. On the other hand, the high-contrast points correspond to multi-layers. A number of sharp lines also can be seen dividing up the film (red arrows). Enlargements at x 12,000 magnification clearly show the hexagonal geometry constructed by these lines and indicating the graphene domains. The domain size was estimated to be 4-5 μm on average, which is almost as fine as the LIT spatial resolution of LIT (2-3 μm). Thus, although the DB defects in a polycrystalline graphene cannot be spatially resolved in LIT, it reveal the presence of DB defects that caused the heat generated. To spatially identify the electrical properties at boundary sites, relatively large domains covering several tens of micrometre are required.

Section S2. Wrinkle in polycrystalline graphene

Figure S2 shows characterizations of the wrinkle structure discussed in Fig. 2F. The micro-Raman mapping was carried out in x/y steps of 1 μm and a CCD integration time of 0.5 s. The scanning area was the same as in the AFM image. At the location of the wrinkle, the G-band intensity

increases because of the larger number of layers. On the other hand, no wrinkle can be observed in the I_D/I_G image.

Section S3. Characterization of epitaxially grown graphene sheets

Figure S3 shows optical microscope images of epitaxially grown graphene film transferred onto a quartz substrate. Single graphene domains having hexagonally symmetric shapes are clearly observed in the upper images. The lateral size in these cases was 50-100 μm. The domains are connected in several places (lower figures). Figure S4 is a Raman mapping measurement of two coalesced domains. The conditions of the measurement were an x/y step of 0.5 μm and CCD integration time of 0.5 s. The Raman images reveal the high I_{2D}/I_G and low I_D/I_G properties suggestive of high-quality mono-layer graphene. The line feature shown in the I_D/I_G image corresponds to the DB defect.

Section S4. Numerical simulation of Joule heat image of graphene sheets

The numerical simulation of the experimentally observed lock-in thermal images was conducted based on the power consumption by Joule heating

$$P(x,y) \propto I^2(x,y) \cdot R(x,y) \tag{1}$$

where *P(x, y)*, *I(x, y)*, and *R(x, y)* correspond to the power, current, and resistance at *(x, y)*, respectively. A schematic diagram of the simulation model is shown in Fig. S5A. First, we prepared an *(x, y)* 2D spatial matrix and set *R* values at each corresponding *(x, y)* point. Then, all *I(x, y)* values were numerically analysed under a constant bias (*V*) in the *x*-axis direction. At all cross points, we established boundary conditions based on Kirchhoff's circuit laws, $\nabla \cdot I = 0$. Finally, *P(x, y)* was imaged by calculating Eq. (1).

Figures S5B and C correspond to an example of a structural model and result of a simulation. The model was of cracked graphene, as shown in Fig. 2C. We prepared a 200 x 290 pixel area and

used two resistance values R_{Gr} and R_{Qz} to represent the graphene (blue region) and quartz (white region). The resistances were 10^{-6} Ωcm for R_{Gr} (the theoretical value) and 10^{18} Ωcm for R_{Qz} (from a specification sheet). The simulated $P(x, y)$ shown in Fig. S5C well represents the experimentally observed lock-in thermal image (Fig. 2D). This result indicates that the thermal pattern around a crack strongly reflects the current flow.

Figure S5D-H is a result for three connected graphene domains. In the case of Fig. S5D, it was assumed that no defects formed at the boundaries. In the case of Fig. S5E, it was assumed that boundary defects increased the resistance R_{DB}. The simulation was performed within a 383 x 278 pixel area, and R_{DB} was assumed to be ten times higher than R_{Gr}. Figures S5F and G show the simulated results for conditions Fig. S5D and E, respectively. The properties varied greatly between the two cases. The experimentally observed LIT image in Fig. 4D is more appropriately represented by Fig. S5G than Fig. S5F.

Section S5. Structural characterization of DB

Figure S6 shows SEM and AFM images at the DB overlap (Fig. 5B). The line feature in SEM (red arrow) corresponds to the DB line. The AFM image shows a slightly raised structure less than 1 nm high (the white arrow). From this result, the DB overlap is a more likely reason for this structure rather than wrinkle/ripple that usually shows up as a bump higher than 1 nm.

Section S6. Speed of LIT imaging

Figure S7A shows amplitude images for several accumulation times. The experiment was performed with polycrystalline graphene. For these images with 60 s and 600 s accumulation times, the graphene is well characterized as a non-uniform thermal pattern. A detailed analysis of background counts (Fig. S7B) and line profile (Fig. S7C) clearly shows that LIT visualizes the local heat properties with data accumulation times of a few minutes.

Section S7. Heat broadening of LIT measurement in graphene films

Figure S8 illustrates a cross-sectional analysis of the LIT image focused on the wrinkle site of polycrystalline sample A (Fig. 2). The line shaped thermal pattern induced by the wrinkle has a narrow FWHM of ~4 μm (Fig. S8B). Considering the width of the wrinkle structure (~2 μm), it is consistent with that the conclusion that the FWHM of the LIT peak is limited by the spatial resolution (2-3 μm). This suggests that heat broadening in graphene films makes small contributions in LIT measurements.

Section S8. Direction of defects in LIT measurement

Here let us discuss the effect that the direction of defects in graphene sheets relative to the current flow has on LIT images. Figure S9 indicates the differences in the heat generation mechanism between (A) orthogonal and (B) parallel direction cases. For (A), heat is generated along the defect. This heat pattern results from the electrical resistance. For (B), on the other hand, the thermal patterns are around the defect, and result from the current flow pattern. Thus, LIT can characterize the electrical influences of the defects in both cases. Figure S9C shows an LIT image of a polycrystalline graphene sample that has orthogonal (black arrow) and parallel (red arrow) direction defects (cracks). The observed thermal patterns are consistent with the above considerations.

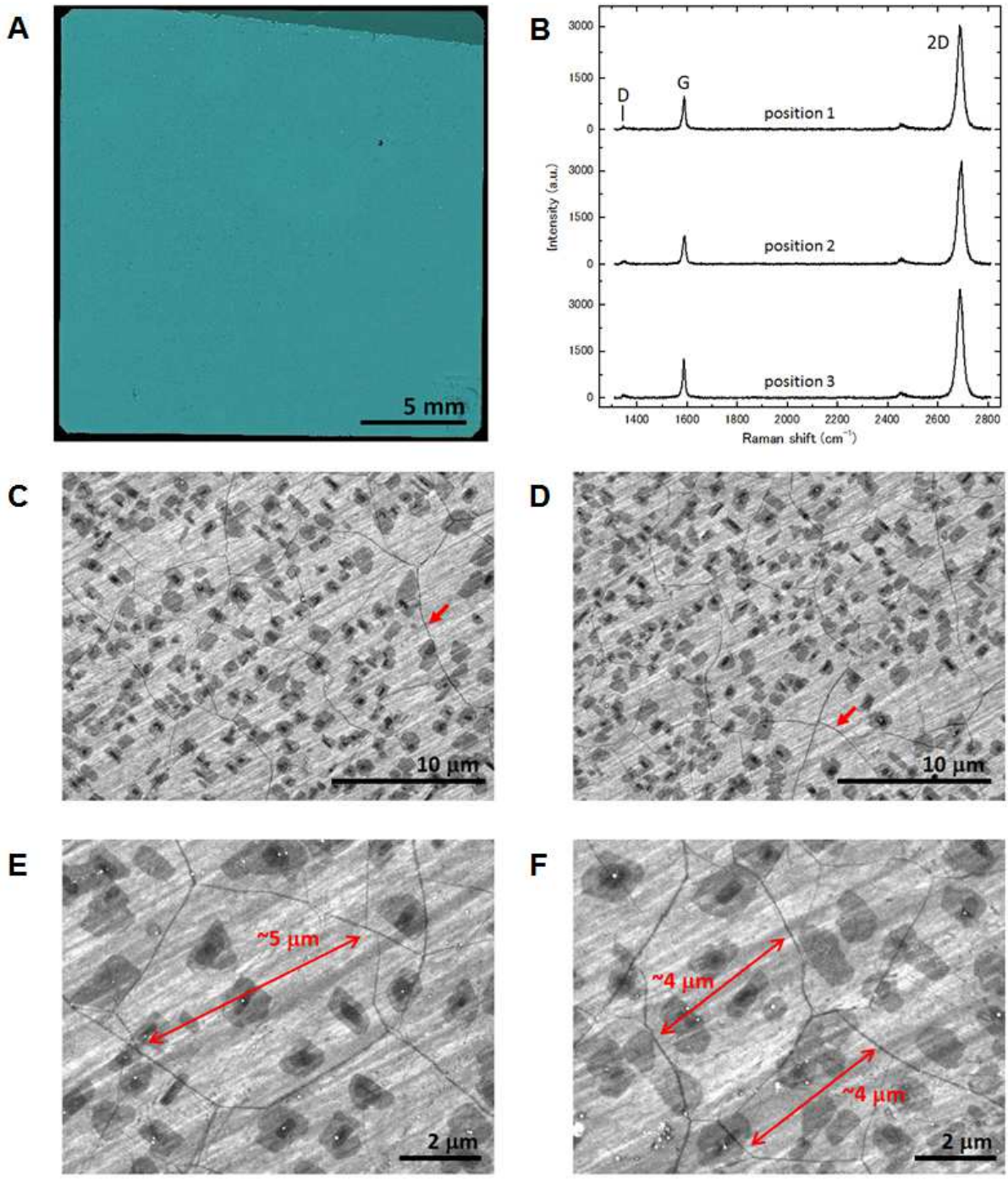

Fig. S1. Optical microscopy image, Raman spectrum, and SEM image of polycrystalline graphene. (**A**) Optical microscope image of graphene sheet transferred onto a quartz substrate. (**B**) Raman spectra from three excitation points. (**C**)-(**F**) SEM images.

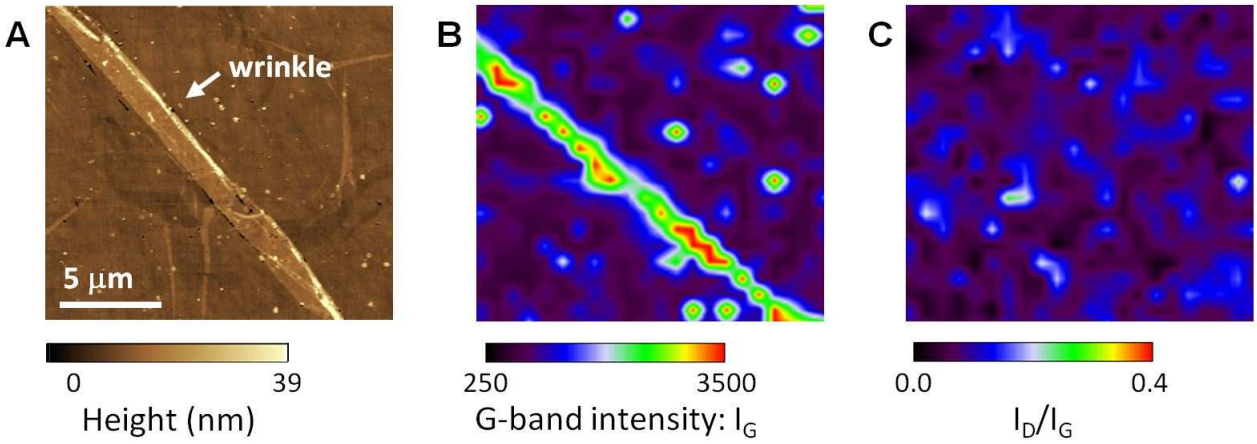

Fig. S2. Structural and optical characterization of wrinkle in polycrystalline graphene. (**A**) AFM image and (**B**), (**C**) Raman mappings of wrinkle structure.

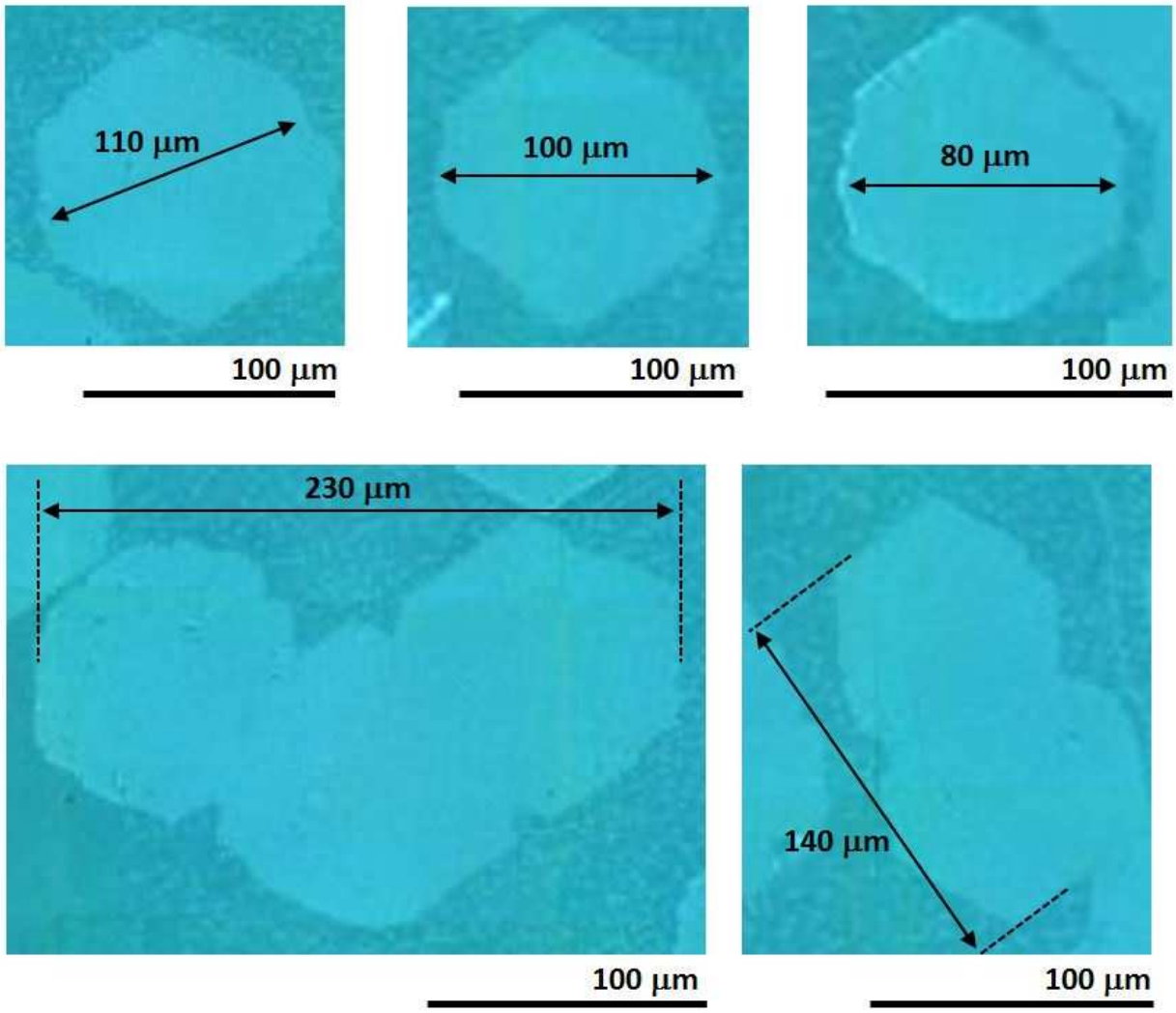

Fig. S3. Optical microscopy image of epitaxially grown graphene domains.

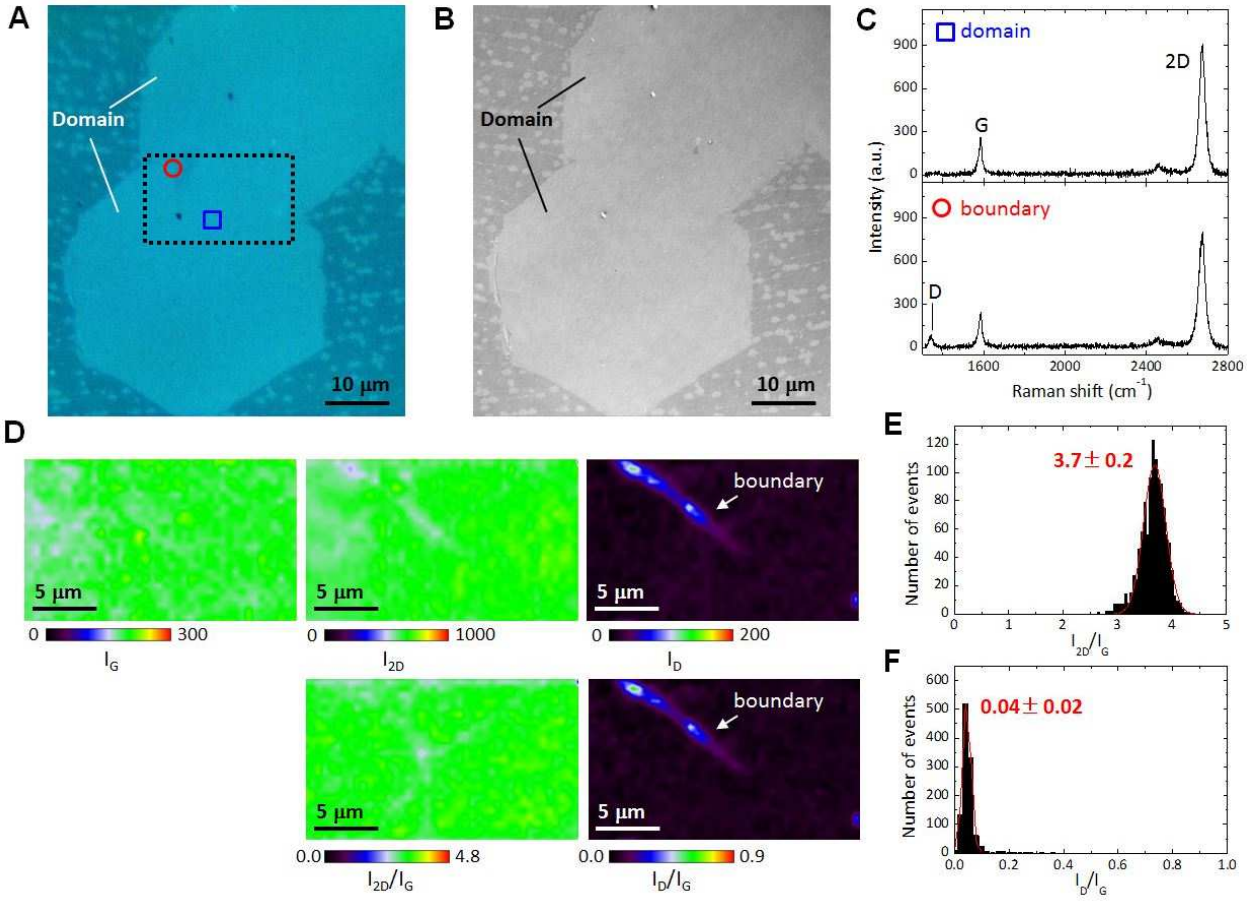

Fig. S4. Micro-Raman spectroscopy with epitaxially grown graphene. (**A**) Optical and (**B**) laser microscope images of connected domains. (**C**) Raman spectra from intra domain (upper) and boundary area (lower). The location of each spectrum is shown as a red circle and blue square in Fig. S4A. (**D**) Results of micro-Raman mapping measurement. The scanning area is indicated by the dashed line in Fig. S4A. Histograms of (**E**) I_{2D}/I_G and (**F**) I_D/I_G obtained by the Raman mapping are also shown. The red lines shown indicate a fitting with a single Gaussian.

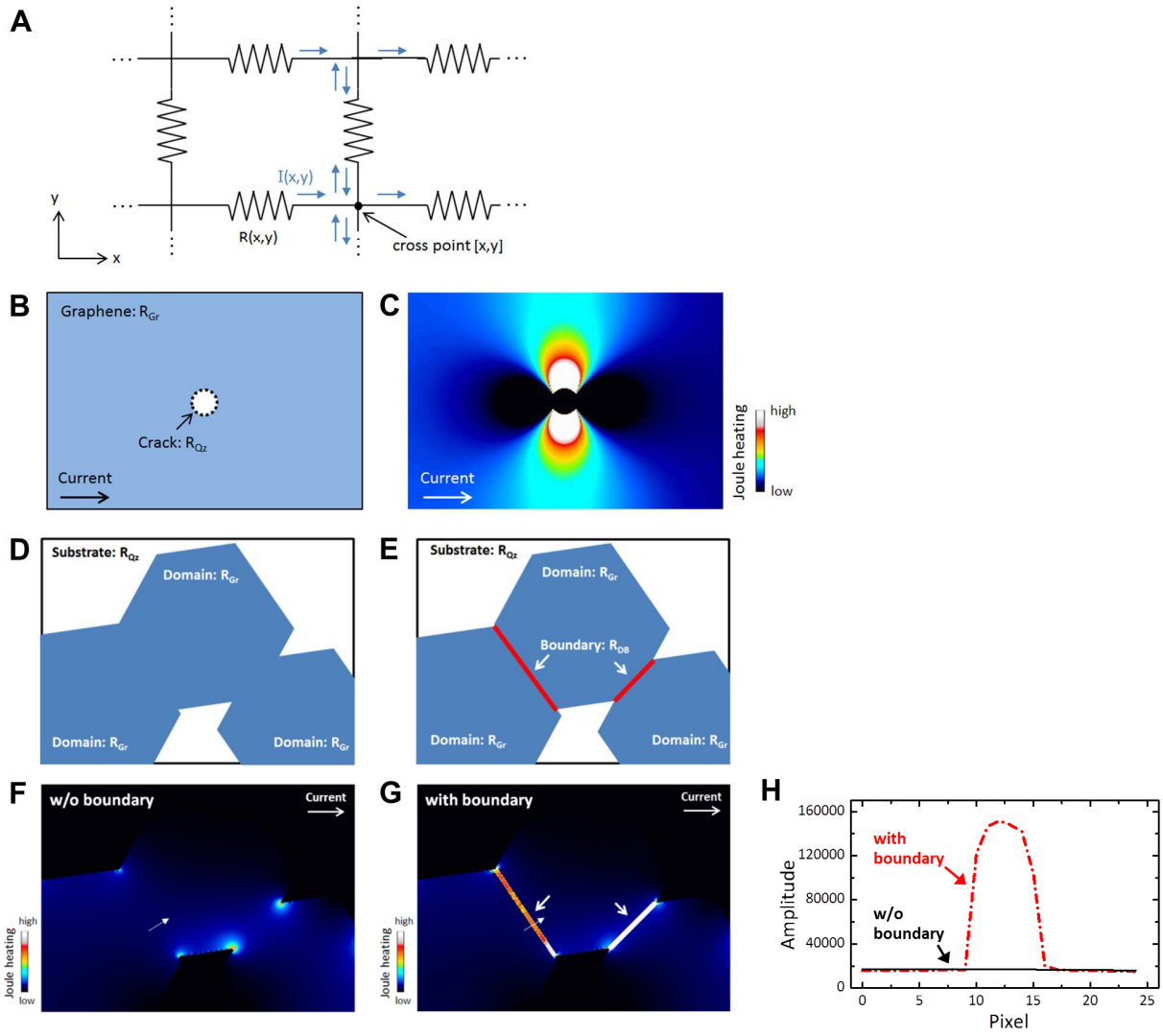

Fig. S5. Simulation of Joule heat imaging. (**A**) Simulation model. (**B**) Assumed graphene structure with crack and (**C**) simulated result. (**D**)-(**H**) Simulation of Joule heating imaging at domain boundary defects. Three graphene domains that coalesced (D) without and (E) with a resistance difference R_{DB} at the boundary. (F), (G) Simulated heat images of Fig. S5D and E, respectively. (H) Line profiles at the boundaries (white dotted arrows in Fig. S5F and G).

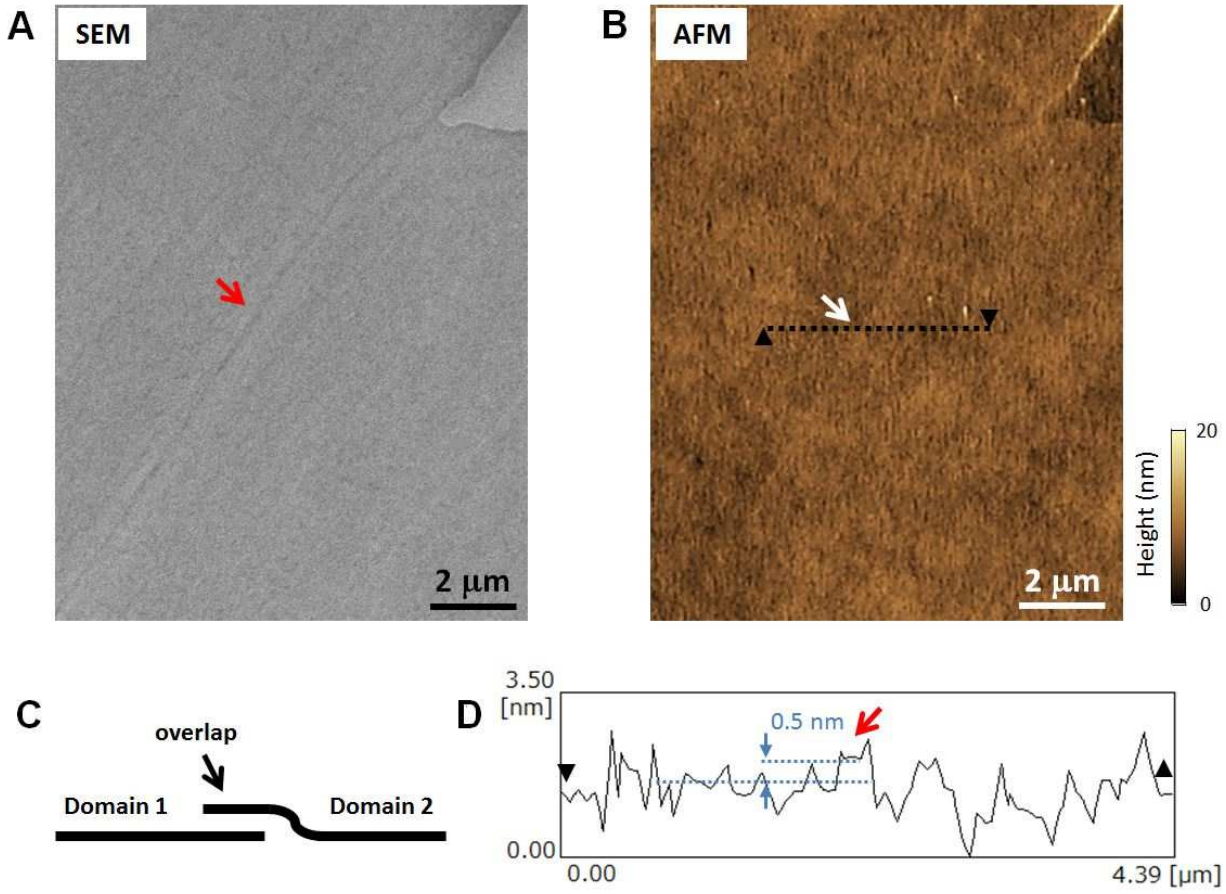

Fig. S6. Structural analysis of overlapped boundary defect. (**A**) SEM and (**B**) AFM images of DB overlap. These images were taken at the same location. (**C**) Schematic diagram of DB overlap. (**D**) AFM cross-sectional profile along black dotted line in Fig. S6B.

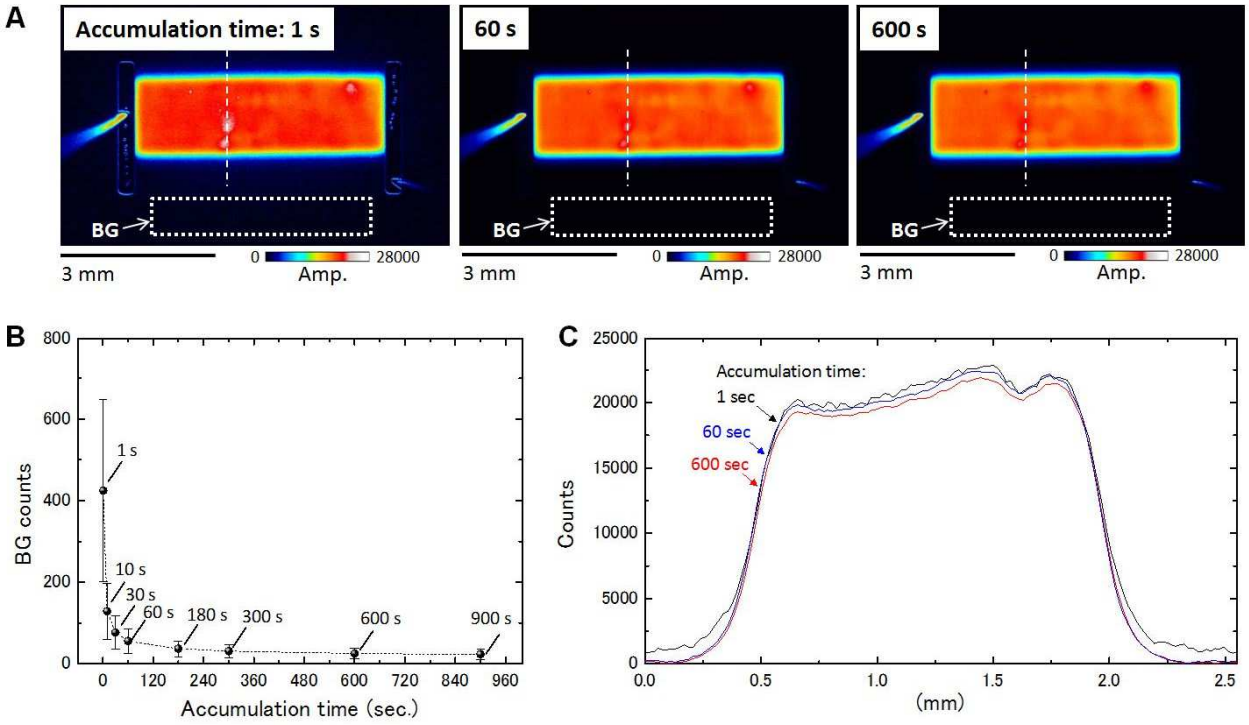

Fig. S7. **LIT image dependence on data accumulation time.** (**A**) LIT image dependence on accumulation time. (**B**) Background count and (**C**) line profile analysis.

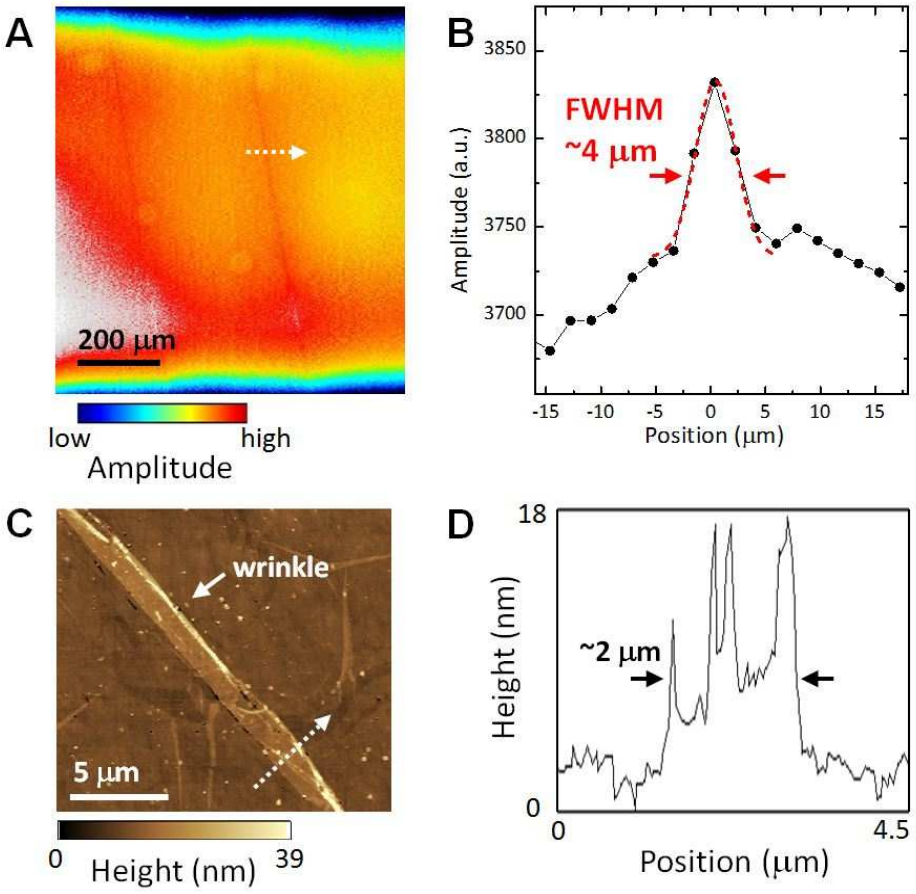

Fig. S8. **Cross-sectional analysis of thermal pattern of LIT.** (**A**) High-magnification LIT image (x8.0) with sample A of polycrystalline graphene. (**B**) LIT cross-sectional profile along the dashed line in Fig. S8A. The red dotted line corresponds to the fitted result with a single Gaussian. (**C**) AFM image of the wrinkle. (**D**) The cross-sectional line profile along the white dashed line in Fig. S8C.

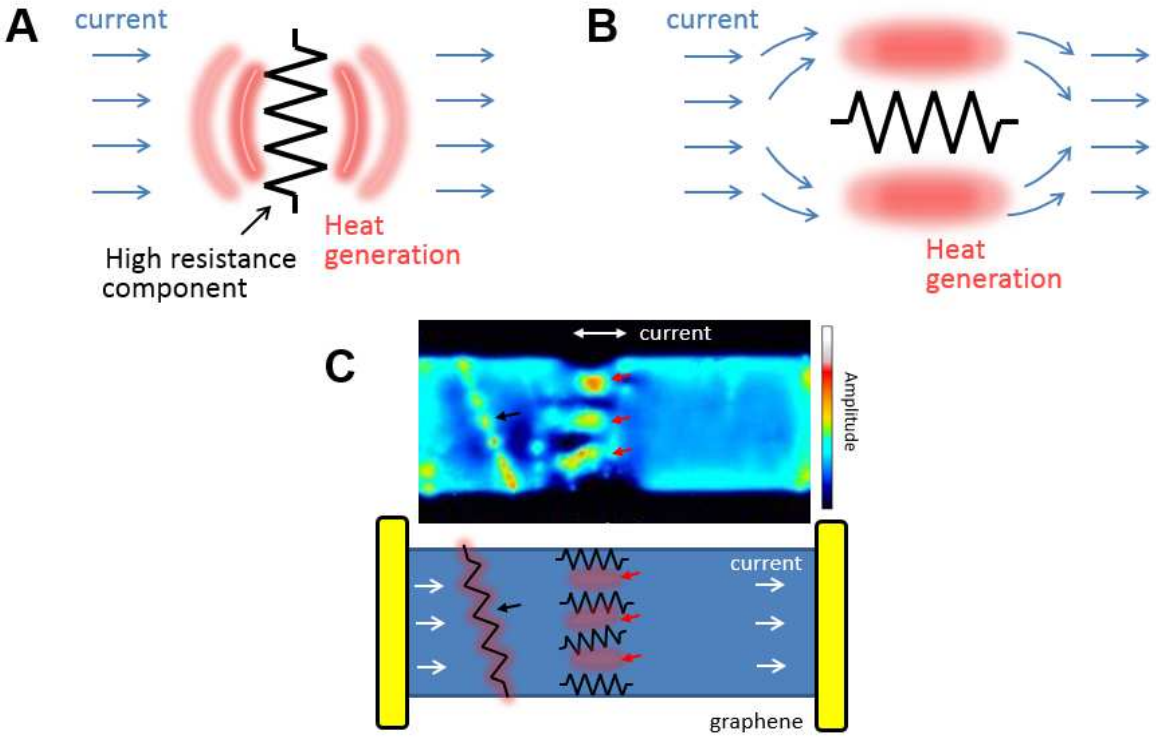

Fig. S9. **Effect of the direction of defects in LIT measurements.** Heat generation mechanism in the (**A**) orthogonal and (**B**) parallel directions of high resistance components. (**C**) LIT image of polycrystalline graphene which has defects in orthogonal and parallel directions.

Table S1. Fitting results of Raman spectrum with polycrystalline graphene. The Raman data are shown in Fig. S1B.

	Pos.1	Pos.2	Pos.3
ω_G (cm^{-1})	1588.0	1587.6	1587.4
ω_{2D} (cm^{-1})	2689.4	2690.0	2689.2
ω_D (cm^{-1})	1347.9	1349.4	1349.4
$FWHM_G$ (cm^{-1})	11.6	11.1	10.9
$FWHM_{2D}$ (cm^{-1})	27.4	28.7	29.2
$FWHM_D$ (cm^{-1})	12.8	16.2	17.2
I_{2D}/I_G	3.20	3.08	2.75
I_D/I_G	0.07	0.11	0.07